In vivo assessment and evaluation of lung tissue morphologic and physiological changes from non-contact endoscopic reflectance spectroscopy for improving lung cancer detection

Yasser S. Fawzy
Mirjan Petek
Perceptronix Medical Inc.
Suite 400, 555 West 8th Avenue
Vancouver, British Columbia V5Z 1C6
Canada

Marjeta Tercelj
University of Ljubljana Medical Hospital Clinical Centre
Centre for Respiratory Diseases
Zaloska 7
1000 Ljubljana, Slovenia

Haishan Zeng
BC Cancer Agency
Cancer Imaging Department
675 West 10th Avenue
Vancouver, British Columbia V5Z 1L3
Canada

Abstract. We present a method for lung cancer detection exploiting reflectance spectra measured *in vivo* during endoscopic imaging of the lung. The measured reflectance spectra were analyzed using a specially developed light-transport model to obtain quantitative information about cancer-related, physiological, and morphologic changes in the superficial bronchial mucosa layers. The light-transport model allowed us to obtain the absorption coefficient (μ_a) and further to derive the micro-vascular blood volume fraction in tissue and the tissue blood oxygen saturation. The model also allowed us to obtain the scattering coefficient (μ_s) and the anisotropy coefficient (g) and further to derive the tissue scattering micro-particle volume fraction and size distribution. The specular component of the reflectance signal and the instrument response were accounted for during the analysis. The method was validated using 100 reflectance spectra measured *in vivo* in a noncontact fashion from 22 lung patients (50 normal tissue/benign lesion sites and 50 malignant lesion sites). The classification between normal tissue/benign lesions and malignant lesions was further investigated using the derived quantitative parameters and discriminant function analysis. The results demonstrated significant differences between the normal tissue/benign lesions and the malignant lesions in terms of tissue blood volume fraction, blood oxygen saturation, tissue scatterer volume fractions, and size distribution. The results also showed that the malignant lung lesions can be differentiated from normal tissue/benign lesions with both diagnostic sensitivity and specificity of better than 80%. [DOI: 10.1117/1.2337529]

Keywords: reflectance spectroscopy; tissue absorption; tissue scattering; tissue blood volume fraction; blood oxygen saturation; tissue oxygenation; tissue scatterer volume fraction; tissue scatterer size distribution; endoscopy; lung cancer detection.

Paper 05187RR received Jul. 15, 2005; revised manuscript received Feb. 15, 2006; accepted for publication Apr. 4, 2006; published online Aug. 25, 2006.

1 Introduction

Lung cancer is the leading cause of cancer death in North America, and it has the second most common cancer incidence among both men and women. Yet, its cure rate can reach more than 90% if it is treated in the early stages. Unfortunately, conventional lung endoscopy (bronchoscopy) based on white light reflectance (WLR) imaging, which is typically used to detect cancer lesions in the central airways of the lung, can only detect about 25% of the lung cancers.[1] This has created the need for detection or imaging modalities that can be accompanied to the white light endoscopy and achieve better diagnostic performance for lung cancer detection. Several research groups have investigated the use of tissue autofluorescence to improve the detection sensitivity of different cancerous lesions and types.[2–9] In addition, a number of fluorescence (FL) imaging systems combined with WLR imaging have been developed and demonstrated significant improvement in the diagnostic sensitivity of the lung cancer in particular.[1,10–13] However, such increase in detection sensitivity was at the cost of the decreased detection specificity. For example, one of the commercial FL imaging systems has achieved a sensitivity of 67% for lung cancer detection, but the specificity was reduced to 66% compared to 90% for WLR imaging alone.[1]

An alternative approach was to perform additional fluorescence and/or reflectance spectroscopic measurements to obtain information about the intrinsic differences in optical properties, which could be used to improve the detection and

Address all correspondence to Yasser Fawzy, Perceptronix Medical Inc., 555 8th Avenue, Vancouver, BC V5Z 1C6 Canada; Tel: 7788954886; Fax: 604-707-0907; E-mail: yfawzy@cpcinc.ca

1083-3668/2006/11(4)/044003/12/$22.00 © 2006 SPIE

classification accuracy of the suspected lesions identified during tissue imaging. Intrinsic differences on optical properties between malignant and benign lesions/normal tissues were found and were related directly to the changes in tissue physiology and morphology that occurred during cancer transformation.[14,15] Clinical spectroscopic measurements and analyses have been performed on various organ sites including the lung.[16–22] In particular, Bard et al.[21,22] have performed spectral measurements and analysis on the abnormal lesions that were identified during fluorescence bronchoscopy and they found significant changes on both absorption-related and scattering-related physiological and morphological properties when tissue became malignant. They have also evaluated the potential of such spectral measurements for improving the specificity for lung cancer detection.[12] However, their measurements were still conducted using a fiber-optic probe inserted through the endoscope instrument channel and been in contact with the tissue surface during the measurement. Recently, we have developed an integrated WLR/FL endoscopy system for simultaneous imaging and noncontact spectroscopy measurements.[23,24] Spectral measurements are performed without introducing a fiber-optic probe through the endoscope instrument channel to touch the tissue surface as in all previous endoscopic spectral measurements, overcoming inconveniences associated with fiber probes and interferences with biopsy forceps and therapeutic tools. This presents great potential for improving the clinical diagnostic sensitivity and specificity at the same time.

In this work we developed a method to obtain quantitative information about cancer-related physiological and morphological changes in lung tissue from reflectance spectra measured with our integrated WLR/FL endoscopic imaging and spectroscopy system. We also investigated the potential of using the so-obtained quantitative information to differentiate malignant lung lesions from normal tissue or benign lesions. In the second section of this article, we describe the *in vivo* spectral measurements with our apparatus and the theoretical foundation of the method used for analyzing the measured reflectance spectra. We then present and discuss the results obtained from the preliminary *in vivo* study performed to validate the proposed method.

2 Materials and Methods

2.1 *In Vivo Reflectance Spectral Measurements*

Reflectance spectroscopy was performed during endoscopic examination using our integrated endoscopy system for simultaneous imaging and spectroscopy described in detail elsewhere by Zeng et al.[23] The bronchial tissue was illuminated by the endoscope with a broad beam (~2 cm beam diameter on tissue). The light source used is a Xenon arc lamp providing both white light (400–700 nm, 10 mW) for WLR imaging and reflectance spectral measurements and a strong blue light (400–460 nm, >50 mW) with weak near-infrared (NIR) light (720–800 nm, 4 mW) for FL imaging and fluorescence spectral measurements. The illumination fiber bundle of the endoscope is interfaced to the light source to illuminate the bronchial tree, and the imaging bundle of the endoscope collects and relays the reflected and the FL signal from the tissue surface to the system for imaging and spectroscopy.

The spectral measurements were performed using a specially designed spectral attachment between the endoscope eyepiece and the camera (Fig. 1). As shown in Fig. 1, the light coming out of the endoscope is focused by Lens 4 to form an interim image at a fiber-mirror assembly. This assembly is fabricated by drilling a hole through a mirror and mounting a 200 μm core-diameter taper fiber through the hole. The 200-μm optical fiber carries the optical reflectance signal or fluorescence signal from a spot at the center of the image, which corresponds to an area of 1-mm diameter at the tissue surface when the endoscope tip is 10 mm from the tissue surface, to the spectrometer (USB2000, Ocean Optics, Dunedin, FL) for spectral analysis. The system spectral resolution is 5 nm. We installed a band-pass (BP) filter (470–700 nm) at the spectrometer entrance to block the reflected blue and NIR light to facilitate fluorescence spectral measurements. As such, the reflectance spectral measurement wavelength range was also restricted to between 470 nm and 700 nm. The spectrometer exposure time was set at 200 ms. The choice of this 200 ms exposure time was determined empirically so that the measured reflectance/fluorescence spectra have good S/N without the risk of movement artifacts. This has also been verified by reviewing video files from randomly chosen 10 patients in a frame by frame fashion and calculated the displacement of our spectral measurement spot during the 200 -ms period (=6 image frames). We found that the displacement is less than 10% of the measurement spot size. The video image and the spectrum, either in the WLR mode or in the FL mode, are displayed simultaneously on the computer monitor in live mode. A still image or a spectrum at any time point of interest during the endoscopy procedure can be captured and stored in the PC. The suspected lesions are identified using FL imaging and/or WRL imaging and then both reflectance and fluorescence spectra are acquired from some of the suspected (identified) lesions. However, in this paper we have only analyzed reflectance spectra. The advantage of this system is that spectral measurements are performed in a noncontact manner through an intermediate image plane. Therefore, no fiber probes are needed to go through the instrument channel of the endoscope as often in other literature, making clinical applications of this technology much more convenient. It also created measurement geometry of broad beam illumination and narrow spot detection, simplifying theoretical modeling of the measured spectra.

The *in vivo* reflectance signal measured from the tissue, $I_{m1}(\lambda)$, can be described as follows:

$$I_{m1}(\lambda) = a_1 I(\lambda) + b_1 I(\lambda) R_{tm}(\lambda), \tag{1}$$

where $I(\lambda)$ is the instrument spectral response, including light source spectral features, fiber-bundle transmittance, and detector efficiency, a_1 is a constant related to the efficiency by which the tissue-surface specular reflection was collected by the probe, b_1 is a constant related to the efficiency of collecting diffuse reflected light from tissue by the measuring probe, and $R_{tm}(\lambda)$ is the true tissue diffuse reflectance to be derived. The reflectance signal measured from tissue $I_{m1}(\lambda)$ was divided by the reflectance signal measured from a reflectance standard disc (WS-1 diffuse reflectance standard, Ocean Optics, Dunedin, FL) to account for instrument spectral response

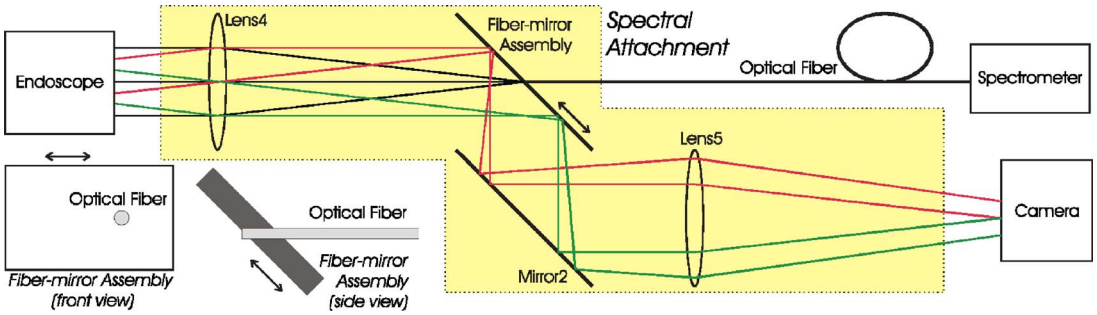

Fig. 1 Schematic diagram of the spectroscopy module attached to the endoscopy imaging system for performing noncontact spectral measurements.

$I(\lambda)$. The reflectance signal measured from the standard disc, $I_{m2}(\lambda)$, can be described as follows:

$$I_{m2}(\lambda) = a_2 I(\lambda) + b_2 I(\lambda) R_s \tag{2}$$

where a_2 is a constant related to the efficiency by which the specular reflection was collected by the probe b_2 is a constant related to the efficiency by which the diffuse reflection signal was collected, and R_s is the reflectivity of the standard disc, which is a constant across the whole visible wavelength range. Dividing Eq. (1) and Eq. (2) and rearranging the equation, we obtained the following:

$$R_m(\lambda) = \frac{I_{m1}(\lambda)}{I_{m2}(\lambda)} = a_0 + b_0 R_{tm}(\lambda) \tag{3}$$

where $R_m(\lambda)$ is the apparent reflectance spectra measured by our apparatus, $R_{tm}(\lambda)$ is the true tissue reflectance spectrum to be derived, and a_0 and b_0 are additive offset and multiplicative factor, respectively, which depend on the measurement conditions during each *in vivo* measurement performed. This includes the amount of specular reflection collected, the material of the standard disc, and the probe distance from the tissue during the measurement.

We performed *in vivo* measurements of normal bronchial mucosa and both benign and malignant lesions on 22 patients. In this pilot study, we obtained a total of 100 spectra. A biopsy sample was obtained for each measurement to classify the measured tissue site into normal, benign, or malignant. The pathology examination of biopsies revealed that 21 reflectance spectra were from normal tissue sites, 29 from benign lesions (26 hyperplasia and 3 mild dysplasia), and 50 from malignant lesions (7 small cell lung cancer, 3 combined squamous cell carcinoma and non-small cell lung cancer, 30 non-small cell lung cancer, 10 adenocarcinoma). Due to the small sample size, our analysis was to develop algorithms to classify the spectra into two groups: (1) malignant lesions for tissue pathology conditions that were moderate dysplasia or worse and (2) normal tissue/benign lesions for tissue pathology conditions that were below moderate dysplasia. This binary classification is also inconsistent with clinical practice that group 1 lesions should be biopsied and treated (or monitored), while group 2 conditions could be left unattended. During routine clinical endoscopy examination all suspected malignant lesions (group 1) should be biopsied while group 2 conditions will not be biopsied. However, in this specially designed study for each patient an extra biopsy (and corresponding spectral measurement) was taken randomly from either a normal-looking area or a suspected benign lesion so that we can assess the performance of the spectral diagnosis relatively independent of the performance of the imaging diagnosis. Five histopathology-confirmed malignant lesions were found by these random biopsies.

2.2 *Modeling of the Reflectance Spectra*

In order to extract quantitative information about cancer-related tissue changes we developed a theoretical model that links the tissue reflectance spectrum measured by our apparatus to specific tissue physiological and morphological parameters related to cancer changes. This was achieved by developing light transport model with its optical absorption coefficient expressed in terms of the micro-vascular related parameters and scattering coefficients expressed in terms of the tissue microstructure scatterer related parameters. The reflectance measurements performed by our apparatus can be represented by an equivalent one-dimensional (1-D) measurement geometry shown in Fig. 2(a). In such geometry a continuous-wave (CW) plane source was irradiating the tissue and the reflectance was detected from a small spot on the tissue surface through a noncontact optical fiber located at an intermediate image plane. The light fluence distribution inside the tissue is a function of depth z only (Fig. 2(b)).

Theoretically, the tissue reflectance spectra $R_t(\lambda)$ at each wavelength can be obtained using Fick's law:

$$R_t(\lambda) = \left.\frac{-j(z,\lambda)}{I_0}\right|_{z=0} = \gamma^{-1} \nabla \phi(z,\lambda)|_{z=0}, \tag{4}$$

where ϕ is the light fluence spatial distribution, j is the diffuse flux, I_0 is the incident power, and γ is the diffusion constant, which depends on the tissue optical properties. The light fluence ϕ was obtained from the general diffusion approximation model.[25] The general diffusion equation is different from the standard diffusion approximation model in that it explicitly includes the collimated source in the radiance approximation and it uses the δ-Eddington approximation to model the single scattering phase function, and thus was expected to give better predictions of visible light (470–700 nm) distribution in the lung tissue, which was found to have low albedo value (i.e., $\mu_a \sim \mu_s$). For a CW

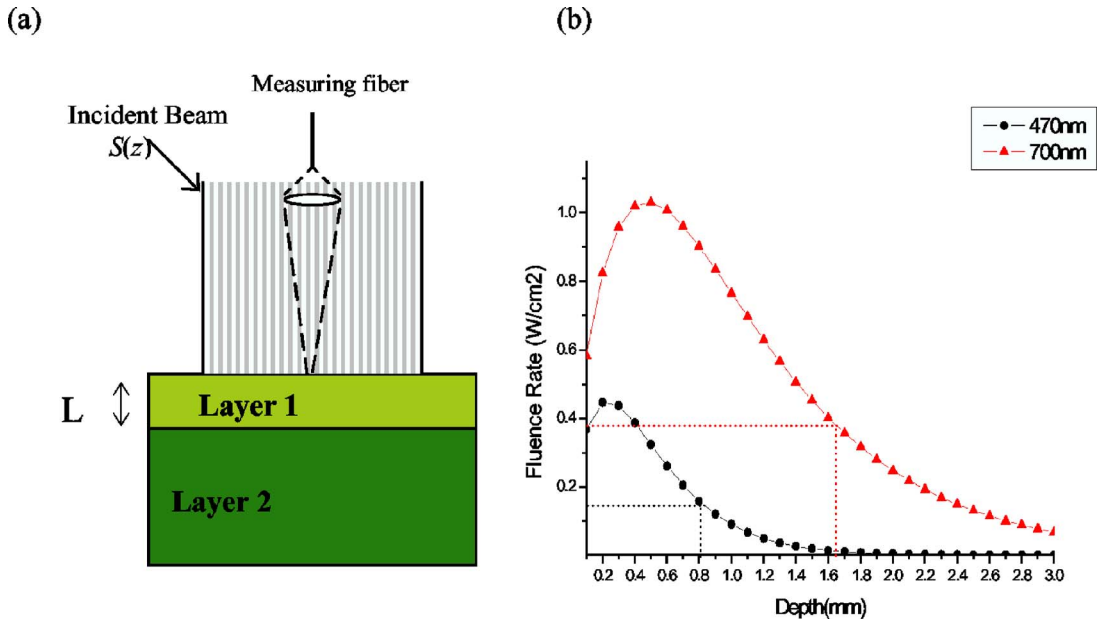

Fig. 2 (a) The equivalent geometry of our endoscopic noncontact spectral measurements. (b) Light fluence distribution as a function of tissue depth, obtained using Monte Carlo simulation in a turbid media with optical properties typical to the lung tissue and a 4% blood content.[27] The fluence becomes insignificant (reduced by factor e^{-1}) for depths after 0.8 mm and 1.6 mm for $\lambda=470$ nm and $\lambda=700$ nm, respectively.

plane source decaying exponentially in the z-direction, the general diffusion model is given by [25,26]

$$\nabla^2\phi(z)-\kappa_d^2\phi(z)=-\gamma S(z),$$

$$\text{with } \kappa_d^2=3\mu_a\mu_{tr}, \quad \gamma=3\mu_s^*(\mu_{tr}+g^*\mu_t^*), \tag{5}$$

where ϕ is the light fluence, $S(z)$ is the incident collimated source term, μ_{tr} is the transport attenuation coefficient equivalent to $[\mu_a+\mu_s(1-g)]$, where μ_s and μ_a are the scattering and the absorption coefficients, respectively. μ_t^* is the total attenuation coefficient and is equivalent to $[\mu_a+\mu_s^*]$. μ_s^* is the reduced scattering coefficient, which is equivalent to $\mu_s(1-f)$, where f is the fraction of light scattered directly forward in the δ-Eddington approximation to the scattering phase function. g^* denotes the degree of asymmetry in the diffuse portion of the scattering. The values of f and g^* were related to the single scattering anisotropy: g from the matching of the second moment of the δ-Eddington phase function to the Henyey-Greenstein phase function,[26] and are equivalent to g^2 and $g/(1+g)$, respectively.[25]

Since we were interested in reflectance spectral signals that were more affected by the superficial mucosa layer (~0.5 mm thickness), within which most early cancerous changes occur, we solved Eq. (5) for the two-layer tissue model (Fig. 2(a)) with the top layer thickness L setting to 0.5 mm. Figure 2(b) shows the light fluence distribution as a function of tissue depth, z, obtained using Monte Carlo simulation. The optical properties of lung tissue used in this simulation were from Ref. 27, and a 4% blood content was added into the tissue model. The fluence becomes insignificant (reduced by factor e^{-1}) for depths after 0.8 mm and 1.6 mm for $\lambda=470$ nm and $\lambda=700$ nm, respectively. Therefore, the measured reflectance signal comes from a tissue volume starting from the surface and up to a depth of 0.8–1.6 mm depending on the wavelength of light. We solved Eq. (5) in the z-direction (1-D) for layer 1 and layer 2, using the index mismatching boundary conditions at interface 1 (air–tissue interface) and the index matching boundary conditions at interface 2 (between the two tissue layers).[26,28] By substituting the solution of Eq. (5) into Eq. (4), we obtained an expression for the tissue reflectance spectrum $R_t(\lambda)$ in terms of the absorption coefficient μ_a, the scattering coefficient μ_s, and the scattering anisotropy, g.

The absorption coefficient, μ_a, was modeled in terms of the blood contents and the absorption coefficient of lung tissue measured *in vitro* with blood drained out. Two parameters were used to describe the blood contents in tissue; the blood volume fraction, ρ, and the blood oxygen saturation, α. The absorption properties of lung tissue *in vivo* can be described by the following equations:

$$\mu_a(\lambda)=\mu_{\text{blood}}(\lambda)\rho+\mu_{\text{in vitro}}(1-\rho),$$

$$\mu_{\text{blood}}(\lambda)=\alpha\mu_{\text{HbO}_2}+(1-\alpha)\mu_{\text{Hb}}, \tag{6}$$

where μ_{HbO_2} and μ_{Hb} are the absorption coefficients for the oxy- and deoxy-hemoglobin, respectively. The *in vitro* absorption coefficient, $\mu_{\text{in vitro}}$, was obtained from the *in vitro* lung tissue measurements made previously by Qu et al.[27]

The scattering coefficient μ_s and the scattering anisotropy g were modeled in terms of the microstructure scatterer volume fractions and size distribution. The tissue scattering model was developed using the fractal approach, assuming that the tissue microstructures' refractive index variations can be approximated by a statistically equivalent volume of discrete micro-scattering particles with a constant refractive index but different sizes.[29,30] The transport scattering coeffi-

cients for a bulk tissue can then be calculated by adding randomly the light waves scattered by each particle together.[26,30] Thus, the transport scattering coefficient and the scattering anisotropy can be modeled using the following integral equations:

$$\mu_s(\lambda) = \int_0^\infty [Q(x,n,\lambda)]\frac{\eta(x)}{\upsilon(x)}\mathrm{d}x \tag{7}$$

$$g(\lambda) = \frac{\int_0^\infty [g(x,n,\lambda)Q(x,n,\lambda)]\frac{\eta(x)}{\upsilon(x)}\mathrm{d}x}{\int_0^\infty [Q(x,n,\lambda)]\frac{\eta(x)}{\upsilon(x)}\mathrm{d}x} \tag{8}$$

where $Q(x)$ is the optical scattering cross section of individual particle with diameter x, refractive index (n), and wavelength (λ). $\upsilon(x)$ is the volume of the scattering particle with diameter x, $g(x)$ is the mean cosine of the scattering angles of single particle. For spherical microparticles, $Q(x)$ and $g(x)$ were calculated from Mie theory using the Mie scattering code by Bohren et al.[31] The volume fraction distribution $\eta(x)$ were assumed to follow a skewed logarithmic distribution;[26,30]

$$\eta(x) = \delta C_0 x^{-\beta}\exp\left(-\frac{(\ln x - \ln x_m)^2}{2\sigma_m^2}\right), \tag{9}$$

where δ is the total volume fraction of all the scattering particles in tissue, β is the size-distribution parameter (fractal dimension) that determines the shape of the volume-fraction size distribution and is related directly to the size of the scattering particles,[26] x_m and σ_m set the center and width of the distribution, respectively, and C_0 is a normalizing factor obtained from the condition $\delta=\int_0^\infty \eta(x)\mathrm{d}x$. The value of x_m was assumed equal to the geometrical mean of (0.05 μm) and (20 μm), which represent the limits of the scattering particles' range of diameters found typically in tissues.[26] Thus $x_m=[(0.05)(20.0)]^{1/2}=1.0$. The width parameter σ_m was assumed to be a constant of 2.0 to match with the fractal scaling range of tissues.[32] Having x_m and σ_m being set, the larger the value of β, the higher the contribution of the smaller-size particles in the scattering particle size distribution function.

The refractive index of the background surrounding media (n_{bkg}) was assumed to be 1.36. The refractive index of the scatterers inside the lung tissue was estimated based on the type of the tissue using the following relation from Schmitt et al.[30]

$$n = n_{\mathrm{bkg}} + f_f(n_{\mathrm{f}} - n_{\mathrm{s}}) + f_{\mathrm{n}}(n_{\mathrm{n}} - n_{\mathrm{c}}) + f_{\mathrm{o}}(n_{\mathrm{o}} - n_{\mathrm{c}}), \tag{10}$$

where f is the fraction and n is the refractive index, and the subscripts f is for collagen fibers, n for nucleus, s for interstitial fluids, o for organelles including mitochondria, and c for intracellular fluids. In this study we have assumed that $n_{\mathrm{n}}=n_{\mathrm{o}}=1.4$, $n_{\mathrm{s}}=1.34$, and $n_{\mathrm{c}}=1.36$.[30] The fibrous-tissue fraction f_{f} value was assumed to be 10% for the first layer (epithelial layer and part of the upper submucosa), and 70% for the second layer, which is constituted of the lower submucosa and the cartilage layer. This results in refractive indexes of $(n_1=1.41)$ and $(n_2=1.45)$ for the first and the second layers, respectively.

2.3 *Inverse Algorithms*

To obtain quantitative information about the blood volume fraction (ρ), the oxygen saturation parameter (α), the scattering volume fraction (δ), and the size-distribution parameter (β) from the measured *in vivo* reflectance spectra $R_m(\lambda)$, we developed a numerical inversion (fitting) algorithm based on Newton-type iteration scheme through least-squares minimization of the function:

$$\chi^2 = \sum_i [R_m(\lambda_i) - (a_0 + b_0 R_t(\lambda_i)\ ]^2, \tag{11}$$

where $R_m(\lambda_i)$ is the reflectance measured at wavelength λ_i, $R_t(\lambda_i)$ is the computed reflectance at wavelength λ_i according to Eq. (4). The iteration procedure were terminated when the χ^2 difference between two adjacent fittings became smaller than 0.01. The following parameters were used as free fitting variables during the inversion process:

- the *blood volume fraction* (ρ) assumed to be the same for both tissue layers;
- the *blood oxygen saturation parameter* (α) assumed to be the same for both tissue layers;
- the *scattering volume fraction* in top and bottom layers (δ);
- the *size-distribution parameters* (β) in top and bottom layers; and
- the *additive and multiplicative terms* in Eq. (3) (a_0) and (b_0).

Using the Marquardt-type regularization scheme,[33] we can obtain the updates of these parameters from the following system of equations:

$$(\zeta^T\zeta + \nu\mathbf{I})\Delta\tau = \zeta^T[R_m - (a_0 + b_0 R_t)], \tag{12}$$

where ζ is the Jacobian matrix, $\Delta\tau$ is the vector updates for the eight parameters $(\rho,\alpha,\delta_1,\delta_2,\beta_1,\beta_2,a_0,b_0)$, $\mathbf{I}$ is the identity matrix, and ν could be a scalar or diagonal matrix.[33] The Jacobian matrix ζ represents the sensitivity of the measured reflectance coefficients on the eight parameters and its elements were computed from the derivatives of $R_t(\lambda)$ with respect to these eight parameters. The inclusion of a_0 and b_0 in the fitting were essential to account for the specular reflection component and the diffuse reflectance probing collection efficiency, which varied for each measurement and depended, among others, on the probe-tissue distance and angle. Thus, the true tissue reflectance (or called "corrected reflectance") $R_{tm}(\lambda)$ can then be extracted from the reflectance spectra measured by the apparatus, $R_m(\lambda)$, using the values of a_0 and b_0 that were obtained from the fitting procedure and substituting in Eq. (3). Of course, all other parameters, ρ, α, δ_1, δ_2, β_1, and β_2 were also derived by this inverse algorithm.

2.4 *Tissue Phantom Experiments*

To verify our modeling approach, we have built a two-layer optical phantom using microparticles with various sizes in order to simulate the scattering properties of tissue microstructures and hemoglobin to simulate tissue blood

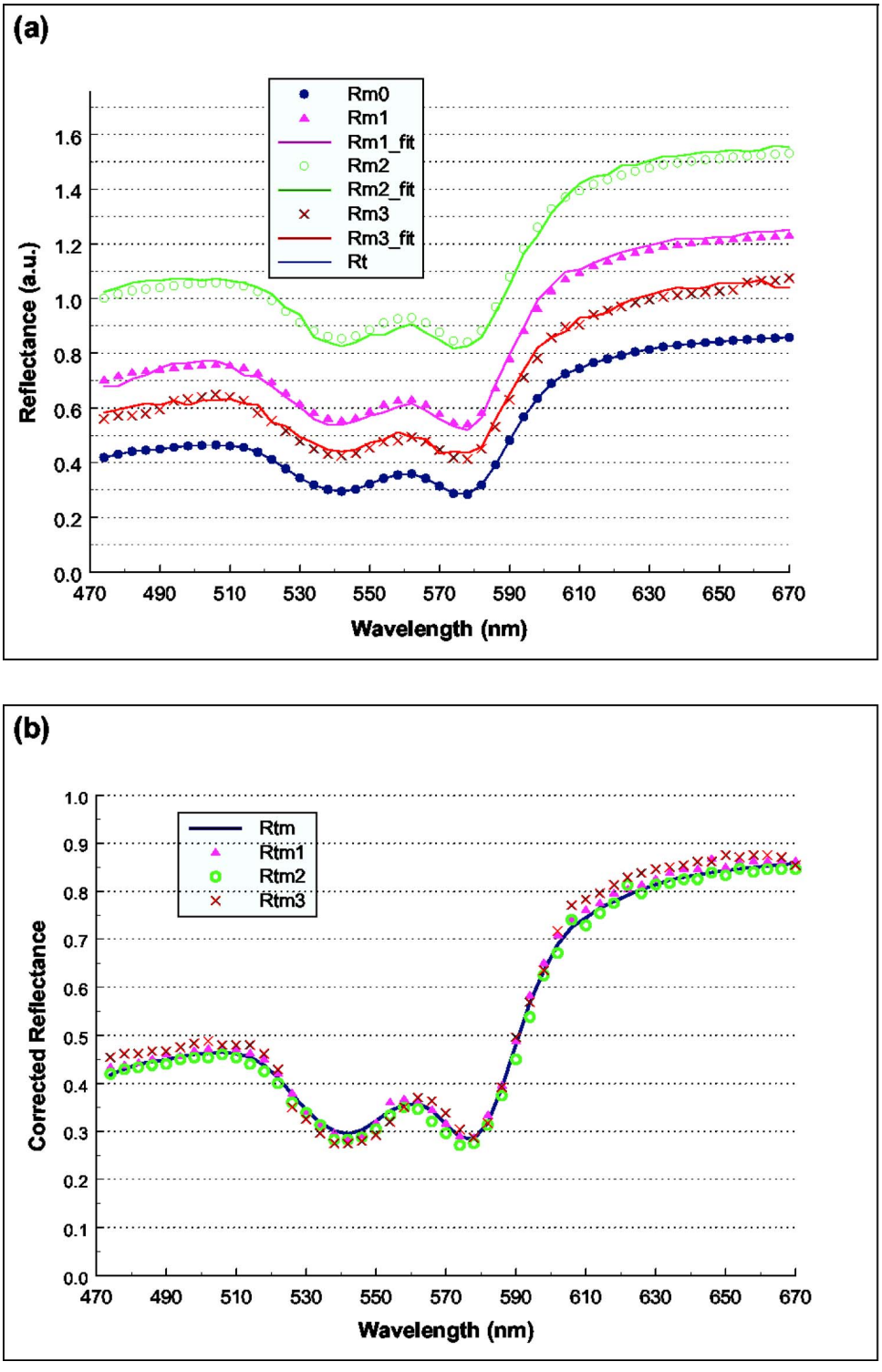

Fig. 3 (a) The measured reflectance spectra, their fitting with our modeling, and the theoretical diffuse reflectance spectrum, R_t of a two-layer tissue phantom consisting of microparticles with various sizes and hemoglobin.[26] R_{m0} is a measurement to avoid the specular reflection, while R_{m1}, R_{m2}, and R_{m3} are measurements with specular reflection contributions and varied endoscope-phantom distances. The symbols are experimental data points, while the curves are model fitting. (b) Corrected reflectance spectra derived from Eq. (3) using the correction coefficient a_0 and b_0, obtained from curve fitting with our developed model. Also shown is the true diffuse reflectance spectrum R_{tm} (=R_t), which is calculated using our forward modeling Eqs. (4)–(8) and the phantom constitution parameters.

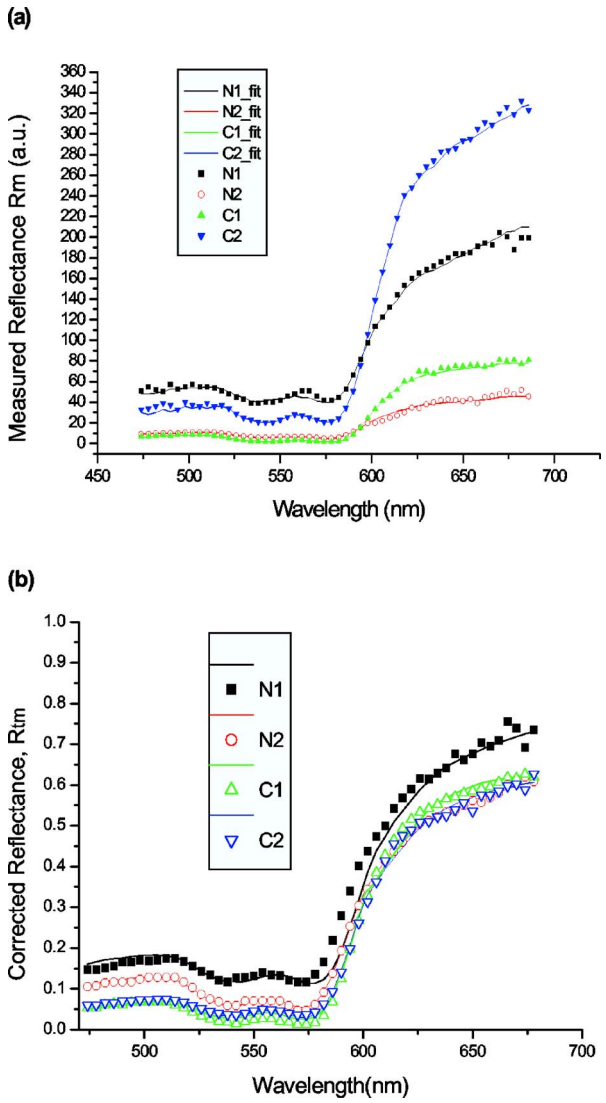

Fig. 4 (a) Reflectance spectra measured (and fitted) from two normal/benign tissue sites and two malignant lesions from the same patient. N1—normal, N2—hyperplasia-diffused, C1—non-small cell carcinoma, C2—another non-small cell carcinoma. The symbols are experimental data points, while the curves are model fitting. (b) True tissue reflectance spectra derived from Eq. (3) using the correction coefficient a_0 and b_0 obtained from curve fitting with our developed model.

absorption.[26] In our previous study, we have carried out experiments on this tissue phantom to verify our modeling approach including comparing the derived scatter volume fraction and scatter size distribution with the phantom constitution. An accuracy of 80% has been achieved.[26] In this study, we used the same tissue phantom to verify the capability of our modeling approach to accurately predict the constant a_0 and b_0, and therefore recover the corrected diffuse reflectance spectrum, R_{tm}.

Our study procedures are as follows:

1. Constitute the tissue phantom and record the blood volume (ρ), oxygen saturation (α), microparticles volume fraction (δ), and size distribution (β).

2. Calculate the theoretical tissue diffuse reflectance R_t using our forward modeling Eqs. (4)–(8) and the recorded parameters in step 1.

3. Measure the diffuse reflectance from the tissue phantom at a fixed distance and angle between the endoscope and the phantom surface. This distance and angle is chosen so that the specular reflectance is completely avoided. The measured spectrum is denoted as R_{m0}. Please note that the specular reflection from the phantom is easy to avoid or capture because the liquid phantom has an ideal flat surface.

4. Perform another three reflectance measurements on the phantom from different distances so that specular reflections contribute to the measured signals. They are denoted as R_{m1}, R_{m2}, and R_{m3}.

5. Correct all the measured spectra by model fitting and compare with the theoretical diffuse reflectance spectrum.

Figure 3(a) shows the measured reflectance spectra, their fitting with our modeling, and the theoretical diffuse reflectance spectrum, R_t. It is obvious that R_{m1}, R_{m2}, and R_{m3} are significantly deviated from R_t because they have included contributions from specular reflection. But they can all be fitted accurately with our modeling approach. As anticipated, R_{m0} is very well consistent with R_t, confirming the validity of our phantom experiment and our forward modeling approach [Eqs. (4)–(8)]. We then replotted R_t as R_{tm} in Figure 3(b), which compares the derived diffuse reflectance spectra (corrected reflectance spectra, R_{tm1}, R_{tm2}, R_{tm3}) from the measured R_{m1}, R_{m2}, and R_{m3} with the true tissue diffuse reflectance spectrum (R_{tm}). We can see that R_{tm1}, R_{tm2}, and R_{tm3} agree with R_{tm} very well, confirming the validity of our whole modeling and experimental measurement approach.

2.5 *Statistical Analysis*

All the fitting results obtained from the 100 tissue spectral measurements were collected and saved in two groups (benign/normal and malignant) for statistical analysis. We used the STATISTICA software package (version 6, StatSoft Inc., Tulsa, OK) for the analysis. While we were not sure if the derived parameters follow normal distributions, the Kolmogorov-Smirnov two-sample test was chosen to evaluate the significance of differences between the two groups (normal tissue/benign lesions vs. malignant lesions) for each of the six parameters $(\rho, \alpha, \delta_1, \beta_1, \delta_2, \beta_2)$ obtained from our fitting results. Discriminant function analysis (DFA) was then applied to the identified diagnostically significant parameters to build diagnostic algorithms for tissue classification. DFA determined the discrimination function line that maximized the variance in the data between groups while minimizing the variance between members of the same group. The performance of the diagnostic algorithms rendered by the DFA models for correctly predicting the tissue status (i.e., normal/benign vs. malignant) underlying each parameter set derived from the reflectance spectrum was estimated using the leave-one-out, cross-validation method on the whole dataset.[34,35] In this method, one case is removed from the dataset and the DFA-based algorithm is redeveloped and optimized using data of the remaining cases. The optimized algorithm was then used to classify the withheld spectrum. This process was repeated until all withheld cases (100 spectra/cases) were clas-

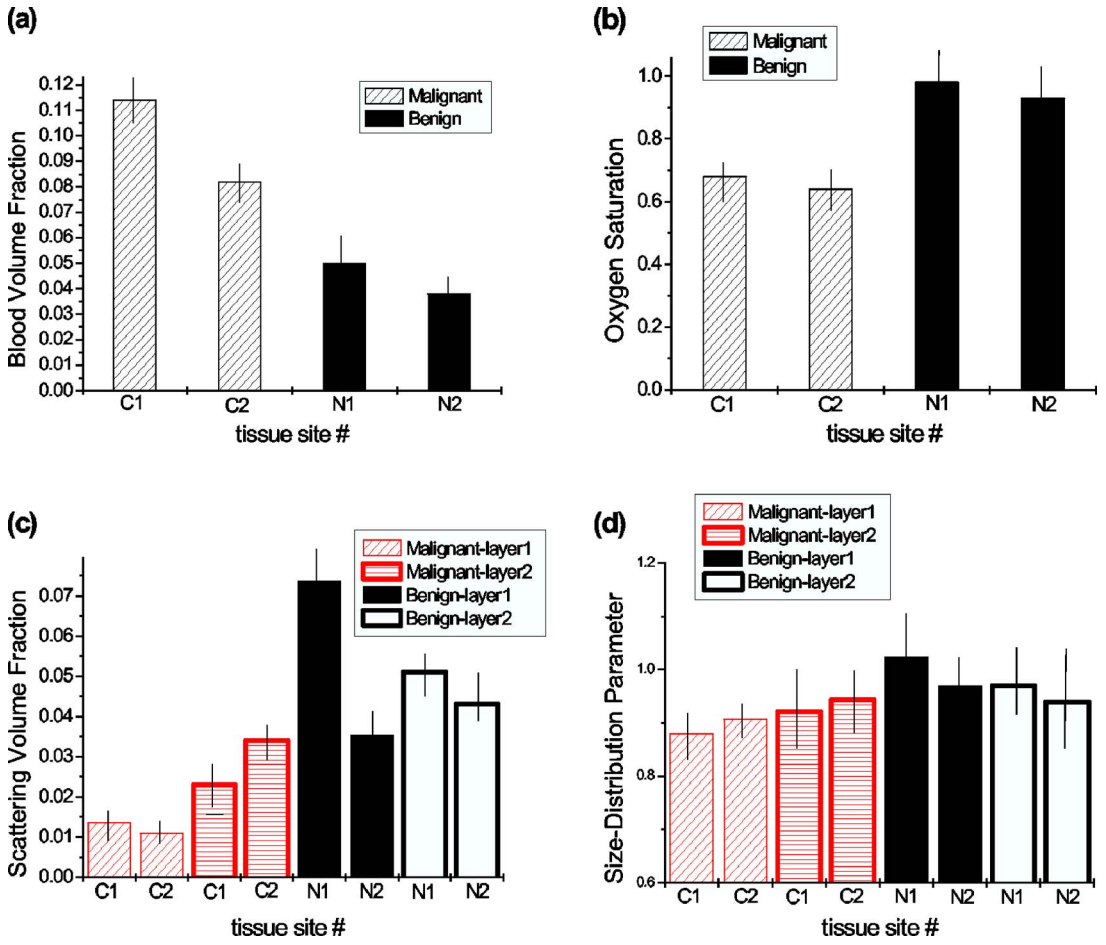

Fig. 5 Absorption and scattering related parameters obtained from fitting the two benign and two malignant spectra in Fig. 4: (a) Blood volume fraction (ρ), (b) tissue oxygen saturation parameter (α), (c) scattering volume fraction in both layers (δ_1 and δ_2), and (d) size-distribution parameter describing the scatterer's size-distribution in both layers (β_1 and β_2). The error bars represented the standard deviations of the fitting parameters derived from the formal covariance matrix of the least-squares fit.

sified. The sensitivity and specificity were calculated from the results of the classification using the following expressions:

$$\text{Sensitivity} = \%\,(\text{Malignant lesions} - \text{False Negative})/\text{Malignant lesions}$$

$$\text{Specificity} = \%\,(\text{Benign lesions} - \text{False Positive})/\text{Benign lesions}.$$

The sensitivity and specificity of imaging diagnosis can also be calculated in a similar fashion by comparing the imaging-based tissue classification results with the histopathology diagnoses.

3 Results and Discussions

In this section we present and discuss the results obtained by analyzing the 100 reflectance spectra measured *in vivo* using the above model and curve fitting. An example of the reflectance spectra measured *in vivo* from two malignant lesions (both are nonsmall cell carcinomas) and two benign tissue sites (one normal tissue site and one hyperplasia-diffused lesion) from the same patient are shown in Fig. 4(a). As can be seen the measured reflectance spectra have large intensity differences, which are related to the variations in the specular reflectance signal and the distance between the endoscope tip and the tissue surface for different measurements. The accuracy of the model fitting to the measured reflectance demonstrated the validity of our proposed method. We have then derived the true tissue reflectance spectra, $R_{tm}(\lambda)$ by correcting the measured reflectance spectra $R_m(\lambda)$ using the fitting results. The corrected spectra, $R_{tm}(\lambda)$ and the fitting of the model are shown in Fig. 4(b). The specular reflection components have been successfully removed and the reflectance intensities fall between 0 and 1 (100%), while the original uncorrected spectra, $R_m(\lambda)$ have quite arbitrary reflectance intensities between 0 and 350%. The fitting results obtained from the analysis of the two benign and the two malignant spectra are summarized in Fig. 5.

The average of the corrected reflectance spectra (R_{tm}) for both the normal/benign group and the malignant group are shown in Fig. 6. It shows that the average reflectance spectra of the normal/benign group have higher intensities in the measured wavelength range (470–700 nm) than the malignant group. These intensity differences are significantly larger for wavelengths above 600 nm. In addition, the two hemoglobin

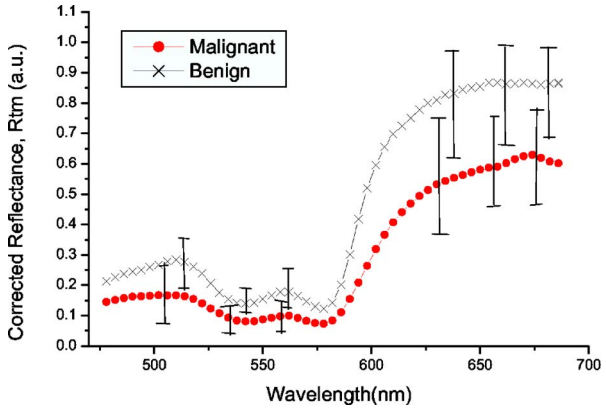

Fig. 6 Average true reflectance spectrum of the 50 normal tissue/benign lesions versus that of the 50 malignant lesions. The error bars are shown for a few data points to give an idea about the degree of the reflectance intensity overlap between the two groups.

absorption valleys around 550 nm and 480 nm are larger and more obvious on the normal/benign group spectral curve than on the malignant group spectral curve. The average fitting parameters $(\rho, \alpha, \delta_1, \beta_1, \delta_2, \beta_2)$ and their standard deviations for the two groups are shown in Table 1. Figure 7 are scatterplots for the values of the bronchial mucosa layer (top layer) parameters $(\rho, \alpha, \delta_1, \beta_1)$ obtained from analyses of the 100 benign and malignant reflectance spectra measured. As shown in Table 1, the mean value of the blood volume fraction was higher for malignant lesions (0.065 ± 0.03) compared to the benign lesions (0.032 ± 0.02). The mean value of the oxygen saturation parameter was reduced from 0.9 for benign lesions to 0.78 for malignant lesions. For the scattering parameters, the mucosal layer showed moderate to significant changes between normal/benign tissues and malignant lesions with the mean values of δ_1 and β_1 for the benign lesions to be 0.077 and 0.97, respectively, compared to 0.048 and 0.91 for the malignant lesions. The scattering parameters (δ_2 and β_2) for the bottom layer showed minimal differences between the normal/benign tissue and malignant lesions. It should be noted that the larger the value of β, the higher the contribution of the smaller-size particles in the scattering particle size distribution function. Thus, an increase in β value indicates a decrease in the scattering particle average size.[26,30] Statistical analysis, using the Kolmogorov–Smirnov two-sample test, showed that the malignant group has significant increase in the blood volume fraction, ρ ($p=0.001<0.05$), significant decrease in the oxygen saturation parameter, α ($p=0.022<0.05$), and significant decrease in the mucosa layer scattering volume fraction, δ_1 ($p=0.013<0.05$) compared to the benign group. The results also showed moderate significant decrease in the size-distribution parameter of the mucosa layer (β_1) in the malignant group compared to the benign group ($p=0.095<0.1$).

The obtained results agree with the results by Bard et al.[21,22] in terms of the significant differences found in the blood volume and the oxygen saturation parameter for benign versus malignant lesions. However, our result seems to have higher absolute values for both parameters. This difference may be related to the higher sensitivity in our measurement geometry to the blood absorption. The broad beam illumination and narrow spot detection geometry in our case samples a deeper tissue volume than their contact fiber probe. It should be noted that the significant increase in the blood volume fraction of the malignant lesions measured in our study agreed with the biological observations that tumors and cancerous tissues exhibit increased microvasculature and accordingly increased blood content.[36] The significant decrease in the blood oxygenation in the malignant lesions is consistent with that hypoxia-related changes occurring during cancerous development,[37] which could be related to the increase in tissue metabolism rate, the lower quality of the tumoral microcirculation, and to the high proliferation rate of the cancerous cells. The significant decrease in the scattering volume fraction found in the measured malignant lesions is consistent with the results obtained by Bard et al.[22,23] for the lung cancer lesions and that obtained by Feld et al.[15] for the colon polyps. The mechanism for such a decrease in the scattering volume fraction is still poorly understood due to the complex nature of the tissue scattering process. However, this may be related to the decrease in the mitochonderial content in cell nucleus,[38]

Table 1 Mean and Standard Deviation of the Six Parameters Related to Tissue Absorption and Scattering for the Normal/Benign Tissue Group and the Malignant Lesion Groups

	Normal/Benign		Malignant		
Parameter	Mean	Std. Dev.	Mean	Std. Dev.	Significance (p)
ρ	0.032	0.02	0.065	0.03	0.001
α	0.90	0.11	0.78	0.13	0.022
δ_1	0.077	0.057	0.048	0.046	0.013
β_1	0.97	0.15	0.91	0.12	0.095
δ_2	0.066	0.048	0.07	0.032	0.25
β_2	0.94	0.12	0.92	0.1	0.65

Note: Also shown are the statistical test results on the significance of the differences between the two groups for these six parameters.

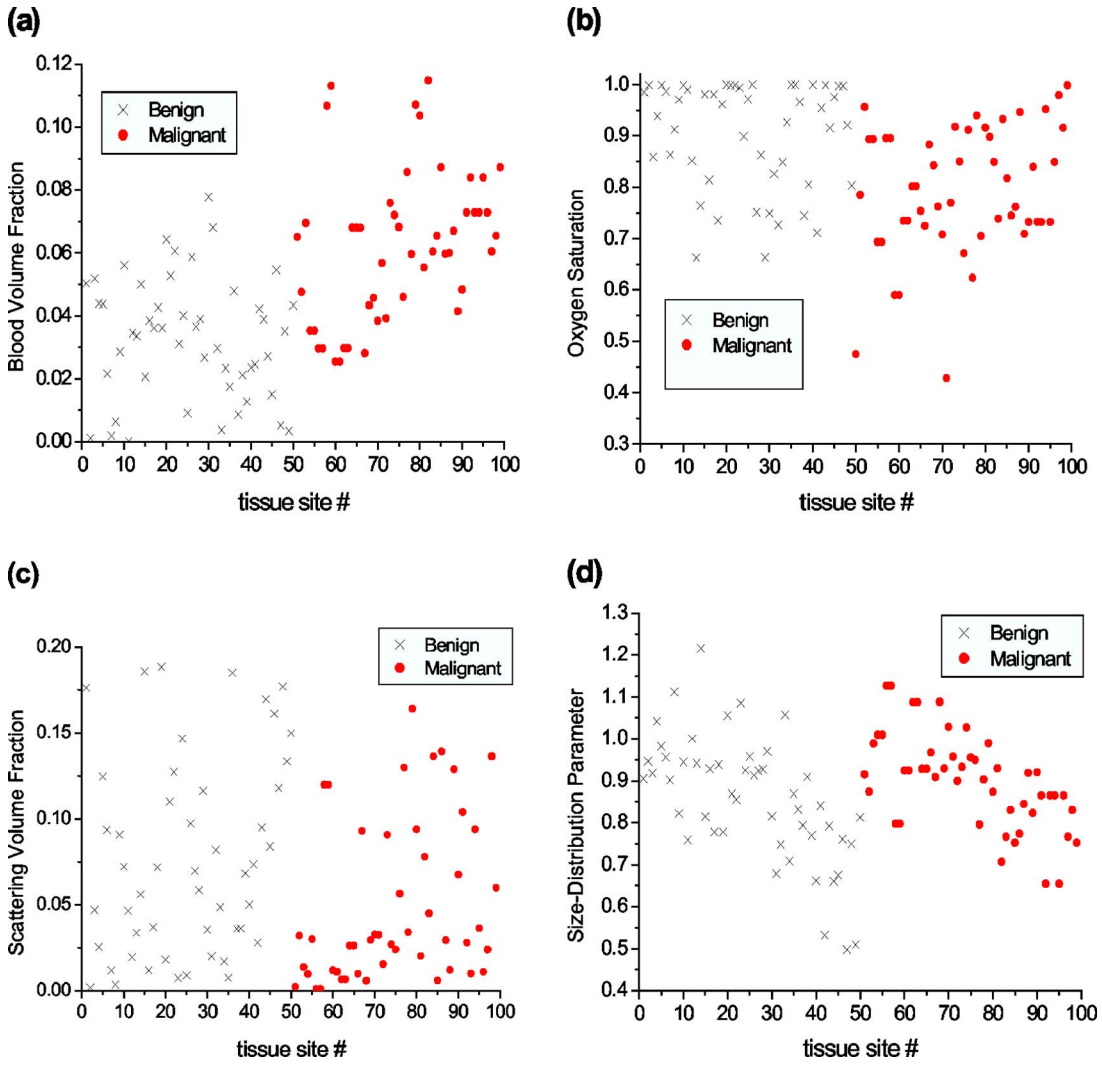

Fig. 7 Scatterplots of the physiological and morphological parameters of the bronchial mucosa layer obtained from the reflectance spectral analysis: (a) Blood volume fraction ρ and (b) oxygen saturation parameter α (c) scattering volume fraction δ_1, and (d) size-distribution parameter β_1.

which have been found to contribute most significantly to the light scattering in the backward (reflectance) directions[39] or to the changes in the refractive index of the cytoplasm due to an increased protein and enzyme content. The size-distribution parameter (β_1) decrease means increased scatterer particle sizes on average for malignant tissues as compared to normal/benign tissues. This is consistent with the fact that cancerous cells have larger nuclei than normal and benign cells.[40]

The results obtained from the DFA showed that the three parameters (ρ, α, δ_1) were significant for the discrimination between the two groups. Figure 8(a) shows the classification results based on measuring the blood volume fraction (ρ) and the scattering volume fraction (δ_1) and (Fig. 8(b)) shows the classification results based on measuring the blood volume fraction and the tissue oxygen saturation parameter. As the figure shows, we can easily identify two domain spaces, with slight overlap, for benign and malignant groups. The DFA results using the three parameters (ρ, α, δ_1) with the leave-one-out, cross-validation method showed that we could differentiate the measured lesions into normal/benign and malignant with sensitivity and specificity of 83% and 81%, respectively. In comparison, we also calculated the sensitivity and specificity of imaging (WLR+FL) diagnosis for the same patient population to be 87% and 43%, respectively. The relative improvement on detection specificity for spectral diagnosis over imaging diagnosis is obvious, and the magnitude of improvement is significant. It should also be noted that the imaging diagnosis is a somewhat subjective procedure that depends on the experience of the attending physician on using fluorescence endoscopy, while the spectral diagnosis presented in this study is a quantitative and objective method.

4 Conclusions

We have successfully developed a light-transport model and numerical method for analyzing *in vivo* tissue reflectance spectra obtained in noncontact measurements to derive quantitative parameters related to tissue morphology and physiology such as the blood volume fraction, the tissue blood oxygen saturation, and the scattering particle total volume

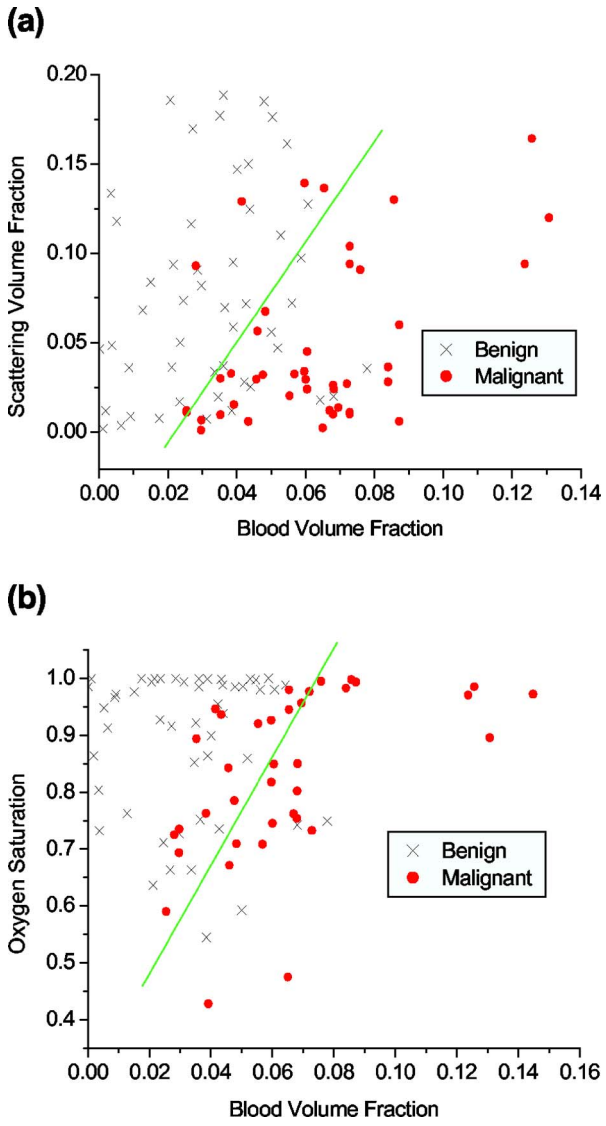

Fig. 8 Binary plot of (a) blood volume fraction ρ versus the scattering volume δ_1, (b) blood volume fraction ρ versus oxygen saturation parameter α.

fraction and size distribution. The method also corrected the effects of the specular reflection and the varying distance between endoscope tip and tissue surface on the clinical reflectance measurements. Our results demonstrated that normal tissue/benign lesions could be discriminated from malignant lesions based on the blood volume fraction, tissue blood oxygen saturation, and the scattering particle volume fraction. The preliminary *in vivo* study using 100 spectra showed that we could detect lung cancers with both sensitivity and specificity of better than 80%, presenting great potential for improving endoscopic lung cancer detection. Future work will involve the application of the method to more *in vivo* measurements and the investigation of combining the reflectance spectroscopy and the fluorescence spectroscopy with the WLR/FL imaging to obtain even better diagnostic sensitivity and specificity for lung cancer detection and localization.

References

1. S. Lam, T. Kennedy, M. Unger, Y. E. Miller, D. Gelmont, V. Rusch, B. Gipe, D. Howard, J. C. LeRiche, A. Coldman, and A. F. Gazdar, "Localization of bronchial intraepithelial neoplastic lesions by fluorescence bronchoscopy," *Chest* **113**, 696–702 (1998).
2. S. Lam, J. Y. C. Hung, S. M. Kennedy, J. C. Leriche, S. Vedal, B. Nelems, C. E. MacAulay, and B. Paclic, "Detection of dysplasia and carcinoma in situ by ratio fluorometry," *Am. Rev. Respir. Dis.* **146**, 1458–1461 (1992).
3. K. T. Schomaker, J. K. Frisoli, C. C. Compton, T. J. Flotte, J. M. Richter, N. S. Nishioka, and T. F. Deutsch, "Ultraviolet laser-induced fluorescence of colonic tissue: Basic biology and diagnostic potential," *Lasers Surg. Med.* **12**, 63–78 (1992).
4. N. Ramanujam, M. Mitchell, A. Mahadevan, S. Thomsen, E. Silva, and R. Richards-Kortum, "Fluorescence spectroscopy: A diagnostic tool for cervical intraepithelial neoplasia (CIN)," *Gynecol. Oncol.* **52**, 31–38 (1994).
5. G. Wagnieres, W. Star, and B. Wilson, "*In vivo* fluorescence spectroscopy and imaging for oncological applications," *Photochem. Photobiol.* **68**, 603–632 (1998).
6. H. Zeng, A. Weiss, R. Cline, and C. MacAulay, "Real time endoscopic fluorescence imaging for early cancer detection in the gastrointestinal tract," *Bioimaging* **6**, 151–165 (1998).
7. C. Wang, H. Chiang, C. Chen, C. Chiang, Y. Kuo, and S. Chow, "Diagnosis of oral cancer by light induced autofluorescence spectroscopy using double excitation wavelengths," *Oral Oncol.* **35**, 144–150 (1999).
8. B. Mayinger, P. Horner, M. Jordan, C. Gerlach, T. Horbach, W. Hohenberger, and E. G. Hahn, "Endoscopic fluorescence spectroscopy in the upper GI tract for the detection of GI cancer: Initial experience," *Am. J. Gastroenterol.* **96**, 2616–2621 (2001).
9. F. Hirsch, S. Prindiville, Y. Miller, W. Franklin, E. Dempsey, J. Murphy, P. Bunn, and T. Kennedy, "Fluorescence versus white-light bronchoscopy for detection of preneoplastic lesions: A randomized study," *J. Natl. Cancer Inst.* **93**, 1385–1391 (2001).
10. M. Leonhard, "New incoherent auto-fluorescence/fluorescence system for early detection of lung cancer," *Diagnostic Therapeutic Endosc.* **5**, 71–75 (1999).
11. D. Goujon, M. Zellweger, A. Radu, P. Grosjean, B. C. Weber, H. van den Bergh, P. Monnier, and G. Wagnieres, "*In vivo* autofluorescence imaging of early cancers in the human tracheobronchial tree with a spectrally optimized system," *J. Biomed. Opt.* **8**, 17–25 (2003).
12. M. P. L. Bard, A. Amelink, M. Skurichina, M. den Bakkerd, S. A. Burgers, J. P. van Meerbeeck, R. P. W. Duin, J. G. J. V. Aerts, H. C. Hoogsteden, and H. J. C. M. Sterenborg, "Improving the specificity of fluorescence bronchoscopy for the analysis of neoplastic lesions of the bronchial tree by combination with optical spectroscopy: Preliminary communication," *Lung Cancer* **47**, 41–47 (2005).
13. Y. Kusunoki, F. Imamura, and H. Uda, "Early detection of lung cancer with laser-induced fluorescence endoscopy and spectrofluorometry," *Chest* **118**, 1776–1782 (2000).
14. J. R. Mourant, A. H. Hielscher, A. A. Eick, T. M. Johnson, and J. P. Freyer, "Evidence of intrinsic differences in the light scattering properties of tumorigenic and nontumorigenic cells," *Cancer* **84**, 366–374 (1998).
15. G. Zonios, L. T. Perelman, V. Backman, R. Manoharan, M. Fitzmaurice, J. Van Dam, and M. S. Feld, "Diffuse reflectance spectroscopy of human adenomatous colon polyps *in vivo*," *Appl. Opt.* **38**, 6628–6636 (1998).
16. H. Zeng, C. MacAulay, B. Paclic, and D. I. McLeant, "A computerized auto-fluorescence and diffuse reflectance spectroanalyser system for *in vivo* skin studies," *Phys. Med. Biol.* **38**, 231–240 (1993).
17. R. J. Nordstorm, L. Burke, J. M. Niloff, and J. F. Myrtle, "Identification of cervical intraepithelial neoplasia (CIN) using UV-excited fluorescence and diffuse-reflectance tissue spectroscopy," *Lasers Surg. Med.* **29**, 118–127 (2001).
18. I. Georgakoudi, E. E. Sheets, M. G. Muller, V. Backman, C. P. Crum, K. Badizadegan, R. R. Dasari, and M. S. Feld, "Trimodal spectroscopy for the detection and characterization of cervical precancers *in vivo*," *Am. J. Obstet. Gynecol.* **186**, 374–381 (2002).
19. M. G. Muller, T. A. Valdez, I. Georgakoudi, V. Backman, C. Fuentes, S. Kabani, N. Laver, Z. Wang, C. W. Boone, R. R. Dasari, S. M. Shapshay, and M. S. Feld, "Spectroscopic detection and evaluation of morphologic and biochemical changes in early human oral carcinoma," *Cancer* **97**, 1681–1692 (1997).

20. J. Qu, C. MacAulay, S. Lam, and B. Paclic, "Laser-induced fluorescence spectroscopy at endoscopy: Tissue optics, Monte Carlo modeling, and *in vivo* measurements," *Opt. Eng.* **34**, 3334–3343 (1995).
21. A. Amelink, H. J. C. M. Sterenborg, M. P. L. Bard, and S. A. Burgers, "*In vivo* measurement of the local optical properties of tissue by use of differential path-length spectroscopy," *Opt. Lett.* **29**, 1087–1089 (2004).
22. M. P. L. Bard, A. Amelink, V. N. Hegt, W. J. Graveland, H. J. C. M. Sterenborg, H. C. Hoogsteden, and J. G. J. V. Aerts, "Measurement of hypoxia-related parameters in bronchial mucosa by use of optical spectroscopy," *Am. J. Respir. Crit. Care Med.* **171**, 1178–1184 (2005).
23. H. Zeng, M. Petek, M. Tercelj, A. McWilliams, B. Paclic, and S. Lam, "Integrated endoscopy system for simultaneous imaging and spectroscopy for early lung cancer detection," *Opt. Lett.* **29**, 587–589 (2004).
24. M. Tercelj, H. Zeng, and B. Palcic, "Acquisition of fluorescence and reflectance spectra during routine bronchoscopy examinations using the ClearVu Elite device: Pilot study," *Lung Cancer* **50**, 35–42 (2005).
25. V. Venugopalan, J. S. You, and B. J. Tromberg, "Radiative transport in the diffusion approximation: An extension for highly absorbing media and small source-detector separation," *Phys. Rev. E* **58**, 2395–2407 (1998).
26. Y. Fawzy and H. Zeng, "Determination of scattering volume fraction and particle size distribution in the superficial layer of a turbid medium using diffuse reflectance spectroscopy," *Appl. Opt.* in press.
27. J. Qu, C. MacAulay, S. Lam, and B. Paclic, "Optical properties of normal and carcinomatous bronchial tissue," *Appl. Opt.* **31**, 7397–7405 (1994).
28. R. C. Haskell, L. O. Svaasand, T. Tsay, T. C. Feng, M. S. McAdams, and B. J. Tomberg, "Boundary conditions for the diffusion equation in radiative transfer," *J. Opt. Soc. Am. A* **11**, 2727–2743 (1994).
29. B. Gelebart, E. Tinet, J. M. Tualle, and S. Avrillier, "Phase function simulation in tissue phantoms: A fractal approach," *Pure Appl. Opt.* **5**, 377–388 (1996).
30. J. M. Schmitt and G. Kumar, "Optical scattering properties of soft tissue: A discrete particle model," *Appl. Opt.* **37**, 2788–2797 (1998).
31. C. F. Bohren and D. R. Huffman, *Absorption and Scattering of Light by Small Particles*, Wiley, New York (1983).
32. J. M. Schmitt and G. Kumsr, "Turbulent nature of refractive-index variations in biological tissue," *Opt. Lett.* **21**, 11310–11312 (1996).
33. W. H. Press, S. A. Teukolsky, W. T. Vetterling, and B. P. Flannery, *Numerical Recipes in C*, 2nd ed., Cambridge Univ. Press, Cambridge, UK (1992).
34. R. W. Dillion and M. Goldstein, *Multivariate Analysis: Methods and Applications*, John Wiley and Sons, New York (1984).
35. P. Lachenbruch and R. M. Mickey, "Estimation of error rates in discriminant analysis," *Technometrics* **10**, 1–11 (1968).
36. R. K. Jain, "Determinants of tumor blood flow: A review," *Cancer Res.* **48**, 2641–2658 (1988).
37. M. Höckel and P. Vaupel, "Tumor hypoxia: Definitions and current clinical biologic, and molecular aspects." *J. Natl. Cancer Inst.* **93**, 266–276 (2001).
38. B. Beauvoit and B. Chance, "Time-resolved spectroscopy of mitochondria, cells and tissue under normal and pathological conditions," *Mol. Cell. Biochem.* **184**, 445–455 (1998).
39. J. R. Mourant, T. M. Johnson, and J. P. Freyer, "Characterizing mammalian cells and cell phantoms by polarized backscattering fiber-optic measurement," *Appl. Opt.* **40**, 5114–5123 (2001).
40. M. Gillaud, J. C. le Riche, C. Dawe, J. Korbelik, A. Coldman, I. I. Wistuba, I. Park, A. Gazdar, S. Lam, and C. E. MacAulay, "Nuclear morphometry as a biomarker for bronchial intraepithelial neoplasia: Correlation with genetic damage and cancer development," *Cytometry* **63A**, 34–40 (2005).